Nanotechnology **19** (2008) 295201 (10pp) doi:10.1088/0957-4484/19/29/295201

Two-dimensional array self-assembled quantum dot sub-diffraction waveguides with low loss and low crosstalk

Chia-Jean Wang, Babak A Parviz and Lih Y Lin

Department of Electrical Engineering, University of Washington, Seattle, WA 98195-2500, USA

E-mail: lylin@u.washington.edu

Received 5 March 2008, in final form 6 May 2008
Published 10 June 2008
Online at stacks.iop.org/Nano/19/295201

Abstract

We model and demonstrate the behavior of two-dimensional (2D) self-assembled quantum dot (QD) sub-diffraction waveguides. By pumping the gain-enabled semiconductor nanoparticles and introducing a signal light, energy coupling of stimulated photons from the QDs enables light transmission along the waveguide. Monte Carlo simulation with randomized inter-dot separation reveals that the optical gain necessary for unity transfer is 3.1×10^7 m^{-1} for a 2D (2 μm length by 500 nm width) array compared to 11.6×10^7 m^{-1} for a 1D (2 μm length) given 8 nm diameter quantum dots. The theoretical results are borne out in experiments on 2D arrays by measurement of negligible crosstalk component with as little as 200 nm waveguide separation and is indicative of near-field optical coupling behavior. The transmission loss for 500 nm wide structures is determined to be close to 3 dB/4 μm, whereas that for 100 nm width is 3 dB/2.3 μm. Accordingly, higher pump power and gain would be necessary on the narrower device to create similar throughput. Considering existing nanoscale propagation methods, which commonly use negative dielectric materials, our waveguide shows an improved loss characteristic with comparable or smaller dimensions. Thus, the application of QDs to nanophotonic waveguiding represents a promising path towards ultra-high density photonic integrated circuits.

(Some figures in this article are in colour only in the electronic version)

1. Introduction

While optical and photonic technologies are destined to play a role in emerging state-of-the-art techniques in communications, computing, medicine, industrial manufacturing and consumer goods, the development path is open ended. However, what is certain is that research advances will be brought to bear to engender seamless integration of media, improve the quality of life, and create efficiencies in industry and useful products for the mass market. At the root of the efforts is a need to pair the appropriate materials with specific applications to enable macroscale to nanoscale structures, the latter of which are nominally inhibited by the diffraction limit. As a result, the fabrication of ultra-compact photonic circuits utilizing conventional dielectric waveguiding technology is impaired by high loss and crosstalk with adjacent structures when the width dimension falls below the size of the transmission wavelength [1]. The use of negative dielectric materials, first proposed ten years ago, presents a route to sub-diffraction energy propagation in a 1D fiber [2]. Since then, alternative metal constructs, such as strip waveguides [3, 4], nanoparticle arrays [5, 6], and metal–insulator–metal (MIM) and insulator–metal–insulator (IMI) junctions [7–9], have been theoretically validated to transmit photons based on conversion to plasmons or oscillating electron clouds through light–material interactions.

However, there is generally a tradeoff in mode confinement and propagation length, which is defined as the distance at which the optical power falls to 1/e of the incident value, as well as the overall device dimension necessary to support transmission [3, 7]. Furthermore, experimental findings are limited in scope for negative dielectric waveguides, and they produced diminished throughput compared to simulation results due to difficulties in fabrication and the resistive heating effects inherent to the material [5]. Example measured loss values are 3 dB/1.76 μm for a 200 nm wide $\times$ 50 nm

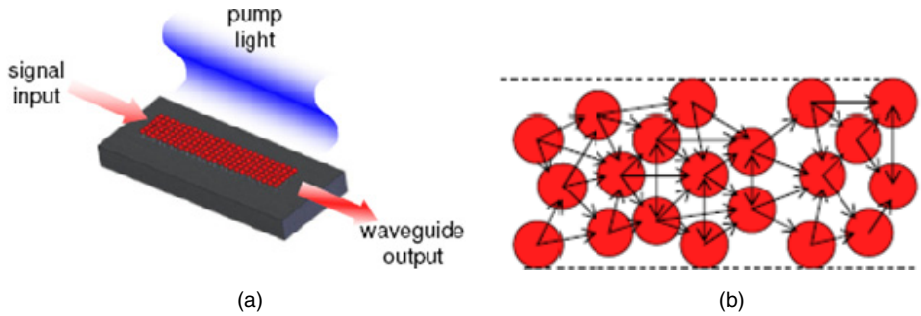

Figure 1. Quantum dot waveguide schematic. (a) An overhead pump source excites electrons to or above the second conduction band state of the QD. After rapid relaxation to the first excited state, the signal light input stimulates photon generation, whose field couples to neighboring particles and prompts further recombination. The chain of photon events leads to transmission of light modified by the pump intensity. (b) Example of cross-coupling near-field energy transfer in a 2D array.

thick gold nanowire [3], 3 dB/1.03 μm for a 300 nm base with 40° angle gold wedge [4], 3 dB/97 nm for a 50 nm diameter silver nanoparticle array with 50 nm inter-dot distance [6], and 3 dB/3.75 μm for a 150 nm wide × 250 nm thick gold insulator–metal–insulator junction embedded in silicon [8]. Additionally, there are nanoscale non-sub-diffraction waveguides [10–14] with improved propagation distances on the order of centimeters or millimeters, although reducing the dimensions below the wavelength cutoff leads to significant crosstalk.

The challenge to guide light at 500 nm and below for variable wavelengths while decreasing the loss is significant. Consequently, we proposed a waveguide consisting of a 1D chain of gain-enabled semiconductor nanoparticles (NPs) placed close together to enable energy transfer via inter-dot coupling [15]. In particular, a pump source generates electron–hole (e–h) pairs in the nanocrystals, which are then prompted by a signal laser to recombine and emit photons at the frequency corresponding to the first excited state. Interaction of the electric field between the NPs further impacts the propagation of the signal light.

Using core/shell quantum dots (QDs) as the basis for a sub-diffraction waveguide, the modeling effort concentrated on calculating the pump power necessary to bring the emission above absorption. With a 5 nm × 5 nm × 5 nm CdSe/ZnS core/shell structure, net linear gain developed between 10 and 100 pW/QD pump power for both pulsed and continuous wave (CW) cases. Secondly, we employed an ABCD matrix approach to simulate the transmission efficiency for a 1D NP array and found a tradeoff relationship between the inter-dot coupling efficiency and unitless gain [16]. Two different self-assembly procedures led to the realization of colloidal QD nanophotonic waveguides on a silicon/silicon dioxide substrate. The first process encompassed four unique binding steps, including hybridization between a base layer DNA with its complementary sequence to deposit quantum dots in a programmable manner. In contrast, a two-layer molecular self-assembly process produced devices with more dense nanoparticle coverage and faster turnaround. Measurement of sub-diffraction QD waveguides made with the latter technique revealed an increase in throughput with larger pump power [17]. While divergence from the original 1D model stemmed from fabrication and test limitations, the result indicated the viability of a larger structure.

Here, we investigate a 2D QD sub-diffraction waveguide by theoretical and experimental methods. Figure 1(a) provides an illustration of the device in which the QDs are assembled in a dense packed array whose width is larger than the nanoparticle diameter, D, thus leading to 2D deposition. While the NP positioning is not well ordered and randomized according to the chemical interactions with each other and the sample surface, figure 1(b) gives an example of the nanoparticle proximity and coverage for a structure with ∼4D width.

The pump and signal sources represent the next key components. The pump laser, whose energy is specified to be equal to or greater than the second excited state for the quantum dot, is directed overhead to excite the quantum confined electrons into the conduction band. By rapid relaxation, the e–h pairs come to occupy the first conduction and valence band states. Subsequently, introduction of the signal light at the first state energy triggers exciton recombination to produce a photon, which may then cause electrons in neighboring QDs to return to the ground state via stimulated emission. Considering the propagation direction, the arrows in figure 1(b) indicate energy transfer between quantum dots and the impact of near-field coupling. Overall, the cascade of photon events leads to signal transmission, which is modified by the pump light and the inter-dot coupling.

In the following sections, we explore a model for estimating the throughput at variable gain levels in a 2D QD nanophotonic array. Beginning with a description of optically induced gain [16, 18], the non-radiative Auger recombination [19, 20] is taken into account to determine the threshold pump intensity. Next, finite difference time domain (FDTD) simulations provide a means of finding the inter-dot coupling efficiency relationship with respect to the position and distance of neighboring particles. Generalizing the two-QD problem to the large number of nanoparticles that form a device is accomplished through multiple cycle Monte Carlo modeling using randomized QD placement. The 2D results are contrasted with the 1D response to show that the gain requirement for the larger structure is reduced. Indeed, comparing the experimental loss behavior of 100 and 500 nm

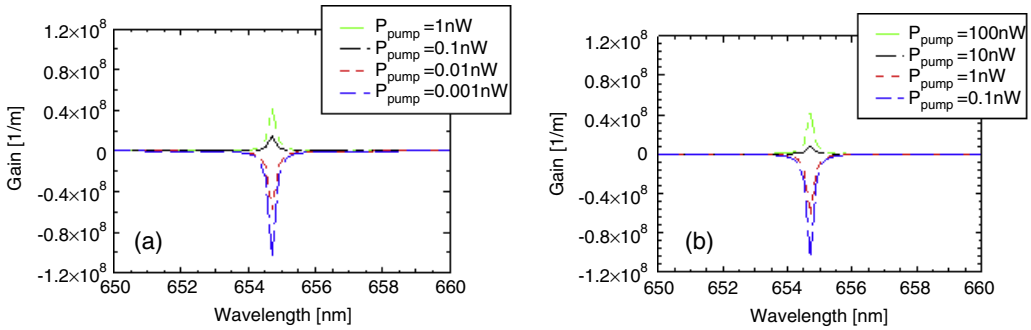

Figure 2. Quantum dot model results. Continuous wave optical pump induced gain simulated as a function of pump power (a) without the Auger process and (b) with an Auger recombination lifetime of 214 ps.

wide lines shows higher signal transfer in the larger arrays. In addition, crosstalk measurements verify the sub-diffraction performance of the quantum dot waveguides.

2. Quantum dot waveguide model

The CW optical gain response of the QD is found primarily through two equilibrium equations, one which balances absorption and emission processes and another which equates the number of holes in the valence band with electrons in the conduction band. The equations are solved simultaneously for the two unknown quasi-Fermi energies in the QD. Then, the gain, which is net emission subtracted by absorption as reflected by the difference between the quasi-Fermi levels, may be fully described given known material constants [16].

The original model provides a foundation to estimate the threshold pump power, optimal gain coefficient, and maximum gain prior to saturation. However, Auger recombination, which is the dominant non-radiative competitive process in the QD, has been observed experimentally [20] and must be included for a more comprehensive result. We previously assumed that, in the biexciton case, the energy released by e–h pair recombination is converted into two photons. In fact there is a finite probability that the energy packet from one photon is transferred to the second exciton, causing the electron or hole to move to a higher energy state. Consequently, the Auger process partially thwarts the transmission of signal light.

To incorporate the described effect requires knowing the time constant associated with a particular NP material and size, which has been observed to follow the relation $\tau_A = \beta R^3$, where R is the particle radius and β is 5 ps nm^{-3} for a QD composed of cadmium selenide. To note, the addition of a capping layer or a shell of zinc sulfide does not appear to affect the trend [20]. Accordingly, using a sphere model to determine the radius necessary for a 655 nm emission QD leads to $R = 3.5$ nm, and $\tau_A = 214$ ps follows. Now, the Auger recombination rate, r_A, may be expressed as

$$r_A = \frac{f_c(E_{1e})[1 - f_v(E_{1h})]}{\tau_A} \times \int_{E_g}^{\infty} \frac{\hbar/\tau_{in}}{[E - (E_{1e} - E_{1h})]^2 + (\hbar/\tau_{in})^2} \, dE \quad (1)$$

where τ_{in} is the intra-band relaxation time describing the broadening of the energy states due to electron–electron collisions, $f_c(E_{1e})$ and $f_v(E_{1h})$ are the quasi-Fermi levels in the conduction and valence bands at the first excited states, E_g is the bandgap energy, and $\hbar$ is the reduced Planck's constant. Hence, equation (1) shows that the non-radiative transfer rate is weighted by the occupation of electrons and holes and has a finite energy distribution. Next, we modify the equilibrium rate equation by adding the r_A term on the emission side:

$$r_{abs,02} = r_{st.ems,20} + r_{sp.ems,20} + r_{sp.ems,10} + r_A \quad (2)$$

to show that, in a three-level system, the absorption rate to the second excited state must counterbalance the spontaneous relaxation process from the second and first states to ground as well as the stimulated emission rate between the first and ground states and the Auger rate.

With the revised equation (2) and the carrier equilibrium equation, which remains the same, the quasi-Fermi energies and gain are recalculated. The outcome is an increase in the threshold illumination pump power from 0.067 nW/QD to 7.8 nW/QD, although the maximum gain at saturation remains the same. The spectra, depicted in figures 2(a) and (b), compare the original and revised curves to show that apart of the difference in required pump to compensate for the non-radiative energy transfer, the trend in gain is identical. The result is expected since the Auger process only impacts the efficiency of optical pumping, leaving the linewidth and the transition energy unchanged. As for the absorbed pump power necessary to excite a quantum dot above threshold, we multiply the absorption of the 405 nm pump wavelength at threshold, calculated to be 3.98×10^7 m^{-1}, with the particle diameter to find that 3.98×10^7 m^{-1} $\times$ 7 nm $= 0.28$ is the fractional absorption and 0.28×7.8 nW/QD gives a required power of 2.16 nW/QD.

From another perspective, the threshold optical intensity as influenced by Auger recombination may be defined as $I_{th} \approx \hbar\omega_p/(\sigma_{abs}\tau_A)$, where ω_p is the pump light frequency and σ_a is the absorption cross section. The latter term, given by the formula $\sigma_{abs} = 2303\varepsilon_\lambda/N_A$ [21, 22], is dependent on the extinction coefficient, ε_λ, as measured in [(M cm)$^{-1}$] units, and Avogadro's constant. From the manufacturer specification of the 655 nm CdSe/ZnS QD extinction ratio, we find $\sigma_{abs} = 2.14$ nm^2, which results in a threshold pump of 2.3 nW/QD and an intensity I_{th} of 1.07 mW μm^{-2} at 405 nm excitation. The same nanoparticles are used in the fabrication such that

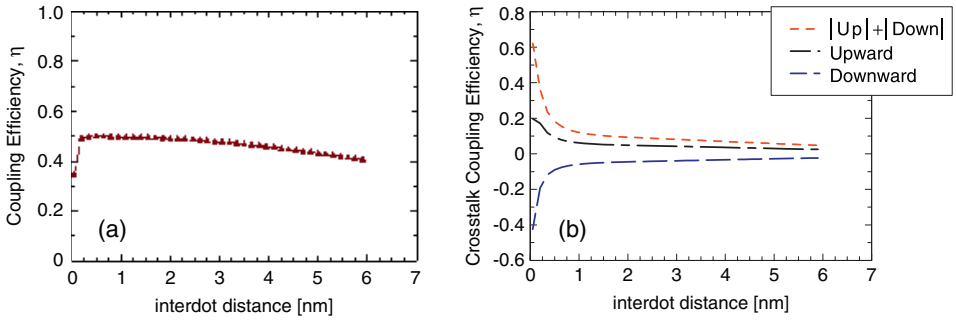

Figure 3. FDTD simulation of inter-dot coupling efficiency variation with respect to dot separation. (a) Coupling in the propagating direction. (b) Cross-coupling in upwards and downwards (lateral) directions.

the resulting pump requirements of 2.16 or 2.3 nW, defined by the gain model or extinction ratio criteria, provide a reference condition in waveguide testing.

2.1. Finite difference time domain inter-dot coupling

Expanding our scope to the dot-to-dot interaction, the coupling efficiency between nanoparticles helps determine the quality of signal throughput. Here, we look to the finite difference time domain simulation [23] for an estimate. Specifically, the QD is modeled as a dielectric sphere embedded with a directional point source representing the stimulated photon emission. Through boundary condition matching, Maxwell's equations for the electric and magnetic fields are solved iteratively across the sample space and over time until a converged solution emerges. The mesh or border size in the simulation volume is a user-defined variable, which trades accuracy of the electromagnetic behavior for computational speed to arrive at a result.

To find the coupling, we use the OptiFDTD v7 package from Optiwave [24], and start with an 8 nm CdSe dielectric sphere at the center of a 20 nm × 20 nm × 20 nm volume. A 655 nm wavelength line source, which is placed at the origin of the QD, is specified with a 0.4 nm full width at half maximum (FWHM) profile directed to propagate forward in the z axis. While the 0.4 nm source leads to higher divergence with respect to distance from the QD, choosing a wider FWHM would result in reduced divergence and lead to a less conservative estimate for inter-dot coupling. For simulation conditions, 5000 time steps of 2.508×10^{-19} s and 3D solutions are specified to find all the x, y, and z components of the electric and magnetic fields. Additionally, the boundary conditions are perfect match layers in x, y, and z, and the polarization of the source is linear in the y (height) direction. Subsequently, the Poynting distribution enables us to calculate the efficiency

$$\eta = \frac{P_{\text{absorb}}}{P_{\text{total}}} = \frac{\int \vec{S} \cdot \vec{\mathrm{d}a}}{\int \vec{S} \cdot \vec{\mathrm{d}A}} \tag{3}$$

as a ratio of power covered by a particular zone compared to that emanating over all space. We define P_{absorb} as the sum of Poynting vectors over an adjacent QD interface along the $+\hat{z}$ propagation direction and P_{total} as the sum of the faces on a box symmetric about the particle covering the top, bottom, front, back, left and right sides. In contrast, the absorbed region entails the only the Poynting values specified at the propagating face within the QD shape boundary.

To optimize for the convergence time using mesh size, η was found for mesh size between 2 and 0.15 nm, such that the cell size varies from 2 nm × 2 nm × 2 nm to 0.15 nm × 0.15 nm × 0.15 nm, respectively. Overall, the FDTD results demonstrate a plateau in the coupling response at the smaller mesh size, and figure 3(a) maps the resulting forward η with respect to the inter-dot distance measured from edge to edge. From the curve, two trends emerge in which the efficiency first increases to 0.5 at a short distance outside the NP due to the spatial distribution of the electric field [25] and then diminishes at further separations. On the other hand, figure 3(b) demonstrates the cross-coupling in the $+\hat{x}$ and $-\hat{x}$ directions (along the width direction of the waveguide), which is indicative of a crosstalk component. The latter value is negative by convention as the energy is flowing down or out of the QD along the negative portion of the y axis. Moreover, the slight asymmetry is attributed to the offset in mesh divisions on the xyz axes over the entire volume.

Förster [26] and optical near-field [27, 28] energy transfer mechanisms provide different routes to determine coupling. However, neither is sensitive to the directional aspect of photons in stimulated emission. Instead, the first method is based solely on an overlap between emission and absorption spectra while the second arises from the effect of the optical field emitted by the QD into the environment and adjacent absorbers as formulated through an exciton–polariton coupling. Therefore, the FDTD-based outcome represents a more effective approach to determining η in the QD waveguide case.

2.2. Monte Carlo transmission simulation

Using the inter-dot coupling curves describing the transfer efficiency between two particles, the transmission characteristics for a system of QDs may now be determined. Through Monte Carlo (MC) modeling, a population of QDs is randomly distributed in a 2D, non-overlapping array. Then, throughput is found by successive calculation of the gain effect and coupling between neighboring nanoparticles as the signal traverses along the propagation direction. By storing the relative output

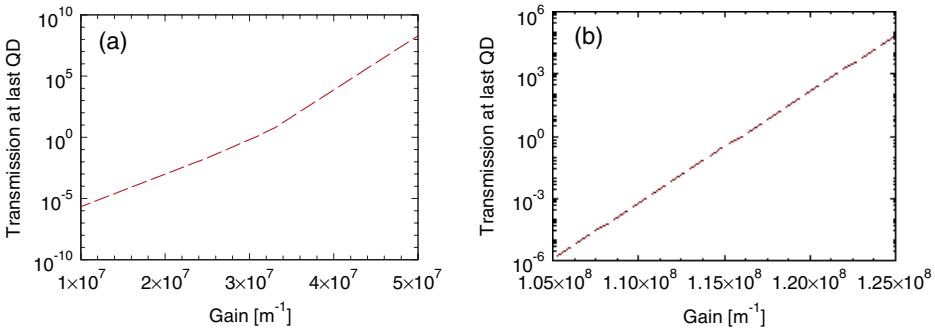

Figure 4. Monte Carlo simulation with randomized inter-dot separations and FDTD-determined coupling profile. Gain-dependent transmission is calculated and averaged over 500 cycles. (a) 2D array result with 155 × 40 particles corresponding to a 500 nm wide, 2 μm long waveguide. (b) 1D array result with 155 particles corresponding to a 2 μm long waveguide.

value from each QD waveguide formation over a large number of cycles, a statistical picture of the device behavior emerges.

Using MATLAB to implement the MC code, we first obtain multiple curve fits to the forward coupling data (figure 3(a)), where the lowest R-squared value is 0.9993, so that points between the mesh can be interpolated. Similarly, the same process for the up and down transfer efficiencies in terms of separation distance, d, result in exponential trends with

$$\eta^{\text{down}} = 0.065d^{-0.4564} \quad \text{and} \quad \eta^{\text{up}} = 0.0674d^{-0.5537}. \tag{4}$$

The R^2 values for equation (4) are 0.9668 for η^{up} and 0.9807 for η^{down}, demonstrating close proximity of the function to the data. Apart from the fitting function, a waveguide length, width, QD diameter, D, and maximum inter-dot distance, $d_{\max}$, are the remaining specifications.

Defining the z and x axes to represent the length and width directions, the y or height component is a fixed magnitude given by the QD diameter across the entire structure. Subsequently, signal transmission at the exiting face of each particle is the sum of three parts, which includes the forward coupling as well as the energy transfer from QDs above and below the one of interest:

$$T_{i,j} = \mathrm{e}^{GD}\left(T_{i-1,j}\eta_{i,j}W_i + \sum_{k\leqslant i} T_{k,j-1}\eta^{\text{up}}_{j-1}L_k + \sum_{k\leqslant i} T_{k,j+1}\eta^{\text{down}}_{j+1}L_k\right). \tag{5}$$

The indices i and j denote the NP's z and x position within the randomized array. Furthermore, summations are used for the cross-coupled terms to account for all relevant neighbors, where L and W act as the overlap coefficients in the lateral and propagation directions and are taken to decrease linearly with the x and z position offset between the original and adjacent particles. Given $D = 8$ nm, the outer factor, e^{GD}, accounts for the gain. As a final modification, the output is weighted by the quantum yield value, $Q_{YD} = 0.86$, as provided by the manufacturer to describe the emission to absorption efficiency.

Using equation (5), which is a recursive formula to simulate staggered propagation, we calculate the gain-dependent output with $d_{\max} = 10$ nm for a 2D QD array of 2 μm length and 500 nm width (corresponding to 155 by 40 particles). The median result for 500 cycles is provided in figure 4(a) over the range of 1×10^7–5×10^7 m^{-1} gain per QD. As may be observed, the relative transmission swings from 10^{-6} to 10^8. However, the crux is that the lossless point settles at 3.1×10^7 m^{-1}, which is below the saturation point provided by the gain result (figure 2(b)) and represents an attainable amount.

To contrast the 2D case with the 1D case, we can reformulate the output at each QD simply as

$$T_i = \mathrm{e}^{GD} \cdot T_{i-1} \cdot \eta_i \tag{6}$$

where only the gain, G, and coupling, η, from the previous particle is relevant. Figure 4(b) depicts the gain-dependent median throughput after adding the quantum yield effect for 500 simulation cycles of a waveguide with 2 μm length (155 × 1 particles), $d_{\max} = 10$ nm and $D = 8$ nm. Unity transmission occurs at $\sim 11.6 \times 10^7$ m^{-1} gain, which is almost four times higher than for the 2D array. The difference demonstrates that at the expense of increased dimensions, a wider waveguide reduces the gain threshold for lossless throughput due to the cross-coupling component. Therefore, depending on the design criteria, array width and desired output amplitude may act as tradeoff variables whereby the Monte Carlo model is useful for predicting the sensitivity and relative degree of improvement.

3. Results and discussion

3.1. QD waveguide behavior

Implementation of the 2D QD waveguide is made possible through a combination of electron beam lithography with self-assembly techniques. Moreover, optimization of the fabrication flow has been accomplished with two-layer chemistry in which carboxylated 655 nm emission CdSe/ZnS core/shell QDs are bound to a substrate via an amine-terminated siloxane compound [17]. The deposition results, as shown for a dual 500 nm wide array spaced at 200 nm, are verified through scanning electron microscope (figure 5(a)), atomic force microscope (figure 5(b)) and fluorescence (figure 5(c)) imaging. Subsequent to manufacture, the device is tested under an optical microscope adapted with tapered

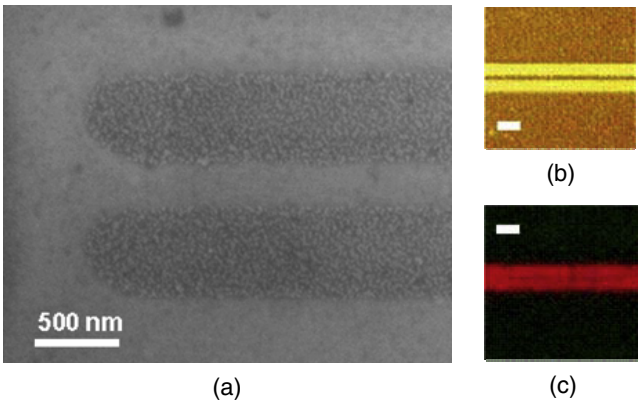

Figure 5. QD dual waveguide of 500 nm width and 200 nm separation. (a) Scanning electron micrograph. (b) Atomic force micrograph. (c) Fluorescence image. The scale bar on (b), (c) is 1 μm.

fiber probes, a collimated pump source, signal source, and supporting equipment including photoreceivers, optical power meters and fiber couplers. Further details of the process and experiment setup are provided in appendices A and B.

Through a customized LabVIEW program, the test system monitors and records the waveguide performance under specific signal and pump source settings. Each data set is a compilation of the output lock-in voltage measured at a fixed time interval for a particular laser setting. We use MATLAB to process the analysis, take averages and standard deviations, and extract any trends. Prior work on 500 nm wide 2D QD arrays showed an increase in transmission at higher pump levels when varied from 0 to 1.4 nW/QD [17]. In contrast, control regions lacking QDs gave insignificant response to the pump variation. Due to the optical chopper and lock-in amplifier, the non-modulated pump source and fluorescence contribution at the signal wavelength are avoided; thus, only the stimulated response at the chopper frequency is detected.

3.2. Loss and crosstalk characterization

To determine the loss figure, we extend the characterization across multiple lengths. The test condition is kept constant except that, immediately after one device is measured, the probe separation and hence the waveguide length is extended and the next test is run to preserve the probe to probe alignment as much as possible. In loss quantification, QD structures from 4 to 10 μm lengths at 500 nm (figure 6(a)) and 100 nm (figure 6(b)) widths were examined.

Varying the pump power per QD from 1.18 to 2.08 nW produced the same upwards trend in transmission at higher optical intensities, where the narrow waveguides revealed steeper slopes. Subsequently, we used an exponential fit to the data since the output power follows the relation $P(z) = P_0 \exp(-\alpha z)$, with respect to the input power P_o and the loss coefficient, α. As a result, we can extract an average loss value of 3 dB per 2.26 μm and 4.06 μm for the 100 nm and 500 nm width waveguides across three pump settings.

Another important aspect to measure for the QD array is crosstalk, which helps to confirm or contradict the sub-diffraction performance. Previous modeling efforts [25] comparing the QD device against conventional dielectric waveguides suggested improved suppression due to the highly distance-dependent cross-coupling efficiency in the NP. In our case, the control test is done with both optical probes aligned to the same structure. Then, one fiber is moved to the adjacent waveguide to detect the signal crosstalk.

Utilizing 500 nm wide devices, figures 7(a) and (b) present the on-waveguide and crosstalk output responses over a 5 μm length array given separations of 500 nm and 200 nm, respectively. Furthermore, figures 7(c) and (d) show similar negligible cross-coupling qualities for 2 and 8 μm length nanoparticle structures. The data are normalized to the throughput found at zero pumping; therefore, negative values in the signal are possible, especially in crosstalk where the lack of measured power falls in the detector noise regime.

Indeed, there is no significant response for crosstalk, while the throughput signal tends to increase with higher pump power as measured on the waveguide. However, in figures 7(a), (b) and (d), at the highest levels of pumping, a drop in the transmission is seen. The event may be attributed to photobleaching of the QDs due to extended exposure to the excitation source [29]. The red crossbars on the crosstalk data bound the error bars, calculated as the standard deviation around the average value.

The data presented here demonstrate that the 2D QD waveguide is a low loss and low crosstalk device. Table 1 provides a summary for reported theoretical and experimental findings for all proposed sub-diffraction waveguiding methods. Indeed, we find that with the exception of the gold insulator–metal–insulator junctions, the QD array has the best transmission loss figure. Although the Ag pin 1D fiber, Ag NP

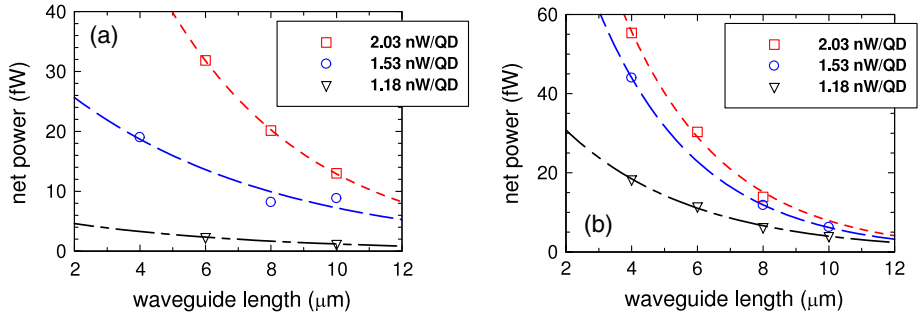

Figure 6. Quantum dot waveguide loss behavior measured over multiple lengths and pump powers. (a) 500 nm wide QD waveguides. (b) 100 nm wide QD waveguides.

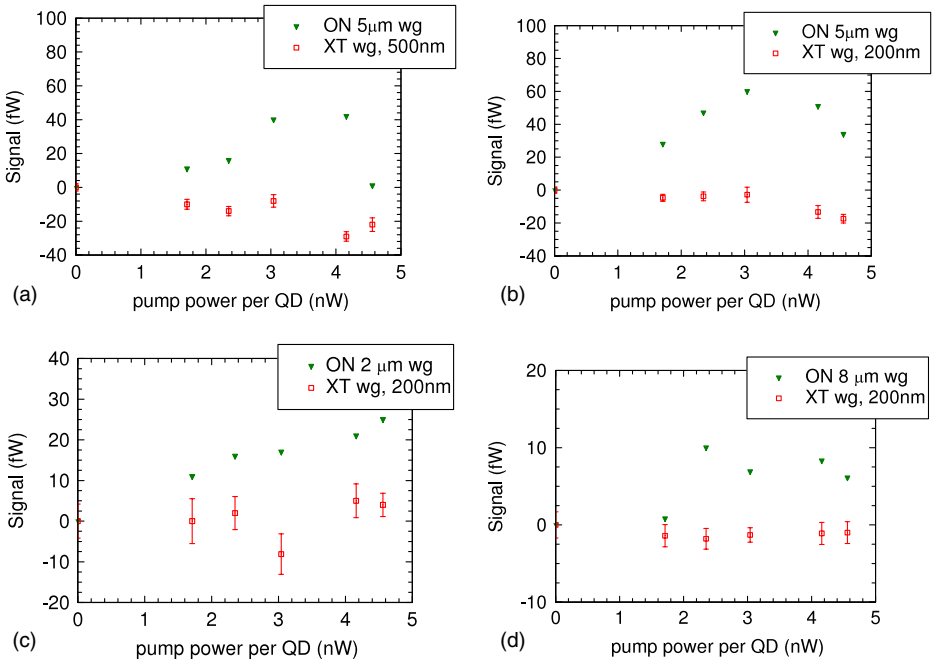

Figure 7. Quantum dot waveguide crosstalk behavior characterized over multiple lengths and pump powers for 500 nm wide structure. (a) 500 nm separation, 5 μm length. (b) 200 nm separation, 5 μm length. (c) 200 nm separation, 2 μm length. (d) 200 nm separation, 8 μm length.

Table 1. A comparison of theoretical and experimental loss for sub-diffraction waveguiding methods.

Method	Device dimensions	Wavelength	Theoretical loss	Experimental loss
Ag pin 1D fiber [2]	20 nm diameter core	633 nm	7.31 dB/μm =3 dB/410 nm	N/A
Au nanowire [3]	200 nm width 50 nm thickness	800 nm	N/A	1.7 dB/μm =3 dB/1.76 μm
Ag wedge [4]	300 nm base 40° angle	632 nm	1.9 dB/μm =3 dB/1.58 μm	2.9 dB/μm =3 dB/1.03 μm
Ag nanoparticle array [5]	50 nm diameter 25 nm inter-dot separation	488 nm	4.8 dB/μm =3 dB/614 nm	N/A
Ag nanoparticle array [6]	50 nm diameter 50 nm inter-dot separation	570 nm	30 dB/μm =3 dB/100 nm	31 dB/μm =3 dB/97 nm
Au IMI [7]	2D coverage 45 nm thickness	1.55 μm	0.000 76 dB/μm =3 dB/3.9 mm	N/A
Au IMI in Si [8]	150 nm width 250 nm thickness	1.55 μm	0.55 dB/μm =3 dB/5.45 μm	0.8 dB/μm =3 dB/3.75 μm
Au clad MIM [9]	150 nm width 100 nm thickness	633 nm	12.2 dB/μm =3 dB/246 nm	N/A
Au clad index-guided MIM [9]	150 nm width 100 nm thickness	633 nm	3.1 dB/μm =3 dB/968 nm	N/A
QD waveguide	500 nm width 100 nm width	639 nm	N/A	3 dB/4.06 μm 3 dB/2.26 μm

array and Au IMI structures have reduced active dimensions, a point to note is that the IMI strip requires an insulating region which increases the effective waveguide size to about 20 μm $\times$ 20 μm [8] while the 1D fiber diameter also increases when accounting for the cladding layer.

4. Conclusions

With the versatility of self-assembly chemistry and the unique 3D confinement and near-field energy transfer properties of semiconductor nanoparticles, the 2D QD waveguide presents a

method for sub-diffraction optical propagation. Concentrating on the theoretical aspect, we started from the fundamental QD component to investigate the gain behavior. In particular, the original CW pump result was modified to account for Auger recombination, the dominant non-radiative competing process to stimulated emission. At the next level, the dot-to-dot interaction was determined through FDTD simulation, which provided a conservative estimate for the coupling efficiency. Extrapolating the two effects into a larger system to mimic the array of randomized NP placement, a Monte Carlo model of the device revealed that the cross-coupling of a 2D structure improves signal throughput for the same gain compared to that for a 1D structure. Alternatively, the gain requirement for unity transmission drops from 11.6×10^7 m^{-1} in the latter to 3.1×10^7 m^{-1} for the former, which is within reach as found by the core/shell sphere QD gain model.

Having established the principle of operation, we used a two-layer molecular self-assembly process to fabricate well-packed arrays of 655 nm emission dots. Device performance was first observed by ramping the pump light to alter the output signal characteristics. Then, measuring the response of multiple waveguides with varying lengths allowed us to investigate the loss as a function of distance. The extracted values of 3 dB/4.06 μm for 500 nm width and 3 dB/2.26 μm for 100 nm width waveguides show an improvement in throughput when compared to prior art sub-diffraction structures using negative dielectric materials, and confirm the trend shown by the Monte Carlo simulation. Furthermore, crosstalk was found to be negligible with as little as 200 nm separation between 500 nm wide waveguides.

While we have realized and demonstrated the 2D QD waveguide, there is room for improvement. Certainly, creating a lossless device of sub-wavelength dimension would be ideal for ultra-compact photonics. As the MC model indicates, increasing gain may compensate for inter-dot coupling inefficiency. Moreover, the required gain levels are attainable prior to saturation from the finite energy states in the QD. What remains is that the pump requirement for the gain must be feasible for the system. With current colloidal NPs, high CW power is necessary to form biexcitons for stimulated emission given the dissipative effect of Auger recombination. Recent work on inverted core/shell particles, where the bandgaps are tailored to separate the hole and electron wavefunctions, makes possible single exciton gain. Thus, the Auger process may be circumvented altogether to enable sub-nW/QD threshold pump [30]. Adopting the type II quantum dots would advance the sub-diffraction waveguide performance beyond reduced loss into an amplified response regime and create more opportunities to form gain enhanced devices at the nanoscale. However, the flexibility of fabrication and the favorable loss results demonstrate the 2D QD array as an effective component for the nanophotonics toolbox.

Acknowledgments

We gratefully acknowledge funding from the National Science Foundation (NSF) ADVANCE program, and UW Royalty Research Fund. C-J Wang would like to thank the NSF Graduate and Intel Foundation PhD Fellowship Programs for financial support. The work was performed in part at the University of Washington Nanotech User Facility (NTUF), a member of the National Nanotechnology Infrastructure Network (NNIN), which is supported by the NSF.

Appendix A. Fabrication of a self-assembled quantum dot waveguide

The 2D QD array nanophotonic waveguides are built upon a silicon dioxide/silicon substrate to promote integration with other Si-based devices. A coupon is cleaved from a wafer and then cleaned by rinsing with xylene, acetone, isopropyl alcohol (IPA) and de-ionized (DI) water and blown dry with nitrogen. In preparation for electron beam lithography (EBL), 3% polymethylmethacrylate (PMMA) is spin-coated onto the surface forming an approximately 90 nm thick layer. The sample is pre-baked at 180 °C for 90 s and then transferred into the SEM vacuum chamber for EBL. Lines of 100–500 nm widths and 2–100 μm lengths are written into the PMMA at dosages of 0.3 to 0.4 nC cm^{-1}. Immersion in 1:3 methyl isobutyl ketone (MIBK):IPA for 70 s followed by an IPA rinse and N_2 drying step develops the waveguide trenches, whose diffraction patterns may be observed under the optical microscope.

Surface treatment with a two-layer self-assembly process [17] begins with oxygen plasma treatment at 20 W for 60 s following lithography. Subsequently, the coupon is submerged for one minute in 0.1–0.2% v/v 3′aminopropyltriethoxysilane (APTES) mixed in a 95% IPA and 5% DI H_2O solution. Afterwards, the sample is rinsed in IPA to remove excess, unbound molecules and blown dry with N_2. The triethoxysilane component of APTES binds to the hydroxyl groups and presents an amine ($–NH_3$) terminal for further reaction. The self-assembled monolayer is affixed to the surface by curing at 110 °C for 7.5 min. The second self-assembled monolayer is provided by adding a droplet of 125 μM 655 nm wavelength emission carboxylated quantum dots (Invitrogen Molecular Probes Q21321MP) suspended in DI H_2O mixed with 1 mM 1-ethyl-3-(3′dimethylaminopropyl)-carbodiimide (EDC), an amine–carboxyl coupling reagent. The solution is left to react for at least one hour and washed with 1× phosphate buffer solution and 0.3 M ammonium acetate to remove the salts from the buffer and again N_2 dried. The procedure is completed with removal of the PMMA by a 3 min immersion in dichloromethane, CH_2Cl_2 [31], DI H_2O rinse and N_2 dry. Multiple-type QD waveguides [32] may be fabricated with repetition of the two-layer process starting from the PMMA deposition and EBL step. The advantages of the approach include assembly of selective wavelength devices, which allows for increased system complexity, and the further suppression of crosstalk as neighboring NPs of different size will not respond to identical signal sources.

Appendix B. Experimental test setup

To measure the waveguide performance, we adapted a traditional optical microscope setup with input and output

tapered fibers mounted on xyz stages driven by Vernier micrometers to deliver the signal light and measure the device throughput with a photodetector. The probes are aligned to the waveguide edges and optimized with respect to the quantum dot pattern for maximum transmission. The broadband fiber light entry point of the microscope is interchangeable with a collimated continuous wave 405 nm pump source, which allows for flexibility between imaging the sample under bright field and observing the device in operation mode, in which we rely upon the quantum dot fluorescence emission to finely position the optical probes. The original microscope beam splitter was replaced with a dichroic mirror (Chroma z405rdc) to reflect the pump light to the sample and transmit higher-wavelength light to the eye piece and an overhead CCD camera. Additional focusing lenses were placed in the optical path to further narrow the beam diameter and increase the pump intensity on the device area.

To control the signal laser, a shutter (Thorlabs SH05 with SC10 controller) acts as a toggle and an optical chopper (Stanford Research SR540) modulates the 639 nm source at 470 Hz, which enables the lock-in amplifier (Stanford Research SR810) to distinguish the signal throughput from the CW pump. Furthermore, output fluctuations in the laser may be monitored by inserting 99/1 split ratio couplers directly after each source such that the larger or smaller amount of optical power is sent to the waveguide or an optical power meter (Newport 818-F-SL & 1830-C), respectively. The latter data are collected to provide a normalization baseline to determine the device behavior. In terms of photodetection, the lock-in may be connected to either a silicon-based femtoWatt photoreceiver (New Focus 2151) coupled with a colored glass long-pass filter (Melles Griot 03FCG461) to prevent pump saturation or a picoWatt detector (Newport 818-SL). The key consideration is the level of power available to the system as detected by the fiber probes.

Specifically, signal delivery to and detection from the waveguide is highly dependent on the coating material and construction of the tapered fibers. We found that chemical etching with hydrofluoric acid (HF) and an isooctane protection layer improved transmission by 100–1000 fold compared to heat pulling with a fusion splicer [33, 34]. Our optimized input and output probe pairing includes an etched multimode fiber with a 200 μm core (Thorlabs BFL48-200) with a silver metalized single-mode fiber (NT-MDT MF003), which permits maximum signal input with reasonable near-field detection capability.

References

[1] Ishimaru A 1991 *Electromagnetic Wave Propagation, Radiation, and Scattering* (Englewood Cliffs, NJ: Prentice-Hall) pp 76–120

[2] Takahara J, Yamagishi S, Taki H, Morimoto A and Kobayashi T 1997 Guiding of a one-dimensional optical beam with nanometer diameter *Opt. Lett.* **22** 475–7

[3] Krenn J R, Lamprecht B, Ditlbacher H, Schider G, Salerno M, Leitner A and Aussenegg F R 2002 Non-diffraction-limited light transport by gold nanowires *Europhys. Lett.* **60** 663–9

[4] Pile D F P, Ogawa T, Gramotnev D K, Okamoto T, Haraguchi M, Fukui M and Masuo S 2005 Theoretical and experimental investigation of strongly localized plasmons on triangular metal wedges for subwavelength waveguiding *Appl. Phys. Lett.* **87** 061106

[5] Quinten M, Leitner A, Krenn J R and Aussenegg F R 1998 Electromagnetic energy transport via linear chains of silver nanoparticles *Opt. Lett.* **23** 1331–3

[6] Maier S 2006 Plasmonics: metal nanostructures for subwavelength photonic devices *IEEE J. Sel. Top. Quantum Electron.* **12** 1214–20

[7] Zia R, Selker M D, Catrysse P B and Brongersma M L 2004 Geometries and materials for subwavelength surface plasmon modes *J. Opt. Soc. Am.* A **21** 2442–6

[8] Chen L, Shakya J and Lipson M 2006 Subwavelength confinement in an integrated metal slot waveguide on silicon *Opt. Lett.* **31** 2133–5

[9] Kusunoki F, Yotsuya T, Takahara J and Kobayashi T 2005 Propagation properties of guided waves in index-guided two-dimensional optical waveguides *Appl. Phys. Lett.* **86** 21110

[10] Law M *et al* 2004 Nanoribbon waveguides for subwavelength photonic integration *Science* **305** 1269–73

[11] Xu Q, Almeida V R, Panepucci R and Lipson M 2004 Experimental demonstration of guiding and confining light in nanometer-size low-refractive-index material *Opt. Lett.* **29** 1626–8

[12] Bogaerts W, Baets R, Dumon P, Wiaux V, Beckx S, Taillaert D, Luyssaert B, Van Campenhout J, Bienstman P and Van Thourhout D 2005 Nanophotonic waveguides in silicon-on-insulator fabricated with CMOS technology *J. Lightwave Technol.* **23** 401–12

[13] Johnson S G, Villeneuve P R, Fan S and Joannopoulos J D 2000 Linear waveguides in photonic-crystal slabs *Phys. Rev.* B **62** 8212–22

[14] Notomi M, Shinya A, Mitsugi S, Kuramochi E and Ryu H-Y 2004 Waveguides, resonators and their coupled elements in photonic crystal slabs *Opt. Express* **12** 1551–61

[15] Wang C-J, Lin L Y and Parviz B A 2004 DNA-directed self-assembled waveguides for nano-photonics *IEEE/LEOS Int. Optical MEMS Conf. Proc. (Kagawa, Japan)* pp 24–5

[16] Wang C-J, Lin L Y and Parviz B A 2005 Modeling and simulation for a nano-photonic quantum dot waveguide fabricated by DNA-directed self-assembly *IEEE J. Sel. Top. Quantum Electron.* **11** 500–9

[17] Wang C-J, Huang L, Parviz B A and Lin L Y 2006 Sub-diffraction photon guidance by quantum dot cascades *Nano Lett.* **6** 2549–53

[18] Klimov V I *et al* 2000 Optical gain and stimulated emission in nanocrystal quantum dots *Science* **290** 314–7

[19] Wang L-W, Califano M, Zunger A and Franceschetti A 2003 Pseudopotential theory of Auger processes in CdSe quantum dots *Phys. Rev. Lett.* **91** 056404

[20] Klimov V I, Mikhailovsky A A, McBranch D W, Leatherdale C A and Bawendi M G 2000 Quantization of multiparticle Auger rates in semiconductor quantum dots *Science* **287** 1011–13

[21] Klimov VI 2000 Optical nonlinearities and ultrafast carrier dynamics in semiconductor nanocrystals *J. Phys. Chem.* B **104** 6112–23

[22] Leatherdale C A, Woo W-K, Mikulec F V and Bawendi M G 2002 On the absorption cross section of CdSe nanocrystal quantum dots *J. Phys. Chem.* B **106** 7619–22

[23] Yee K 1966 Numerical solution of initial boundary value problems involving Maxwell's equations in isotropic media *IEEE Trans. Antennas Propag.* **14** 302–7

[24] Optiwave 2007 OptiFDTD v7 simulation software ©OptiWave Systems Inc., http://www.optiwave.com/

[25] Huang L, Wang C-J and Lin L Y 2007 A comparison of crosstalk effects between colloidal quantum dot waveguides and conventional waveguides *Opt. Lett.* **32** 235–7

[26] Förster T 1959 Excitation transfer *Discuss. Faraday Soc.* **27** 300–20
[27] Sangu S, Kobayashi K and Ohtsu M 2001 Optical near fields as photon-matter interacting systems *J. Microsc.* **202** 279–85
[28] Nomura W, Yatsui T, Kawazoe T and Ohtsu M 2007 The observation of dissipated optical energy transfer between CdSe quantum dots *J. Nanophoton.* **1** 011591
[29] van Sark W G J H M, Frederix P L T, Bol M A A, Gerritsen H C and Meijerink A 2002 Blueing, bleaching, and blinking of single CdSe/ZnS quantum dots *ChemPhysChem* **3** 871–9
[30] Klimov V I, Ivanov S A, Nanda J, Achermann M, Bezel I, McGuire J A and Piryatinski A 2007 Single-exciton optical gain in semiconductor nanocrystals *Nature* **447** 441–6
[31] Hu W, Sarveswaran K, Lieberman M and Bernstein G H 2005 High-resolution electron beam lithography and DNA nano-patterning for molecular QCA *IEEE Trans. Nanotechnol.* **4** 312–6
[32] Wang C-J and Lin L Y 2007 Nanoscale waveguiding methods *Nano Res. Lett.* **2** 219–29
[33] Hoffman P, Dutoit B and Salathé R-P 1996 Comparison of mechanically drawn and protection layer chemically etched optical fiber tips *Ultramicroscopy* **61** 165–70
[34] Lambelet P, Sayah A, Pfeffer M, Philipona C and Marquis-Weible F 1998 Chemically etched fiber tips for near-field optical microscopy: a process for smoother tips *Appl. Opt.* **37** 7289–92